Full Title: The mesodermal source of fibronectin is required for heart morphogenesis and cardiac outflow tract elongation by regulating cell shape, polarity, and mechanotransduction in the second heart field.

Short Title: Role of mesodermal fibronectin in cardiac development

Authors: Cecilia Arriagada and Sophie Astrof*

Affiliation: Department of Cell Biology and Molecular Medicine, Cardiovascular Research Institute, Rutgers Biomedical and Health Sciences, 185 South Orange Ave, Newark, NJ, 07103, USA.

*Author for correspondence: Sophie Astrof, Ph.D.
Phone: 617-429-8295
E-mail: sophie.astrof@rutgers.edu

Abstract

Failure in the elongation of the cardiac outflow tract results in congenital heart disease due to ventricular septum defects and misalignment of the great vessels. The cardiac outflow tract lengthens by the accretion of progenitors derived from the second heart field (SHF). SHF cells in the splanchnic mesoderm are exquisitely organized into an epithelial-like layer forming the dorsal pericardial wall (DPW). Tissue tension within the DPW, cell polarity, and proliferation, are requisite for the addition of SHF-derived cells to the heart and outflow tract elongation. However, genes regulating these processes are not completely understood. Using conditional mutagenesis in the mouse, we show that Fn1 synthesized by the SHF is a central regulator of the epithelial architecture in the DPW. Fn1 expression is enriched in the anterior DPW and mediates outflow tract elongation by regulating cell polarity, shape, cohesion, and mechanotransduction. Our studies establish that Fn1 synthesized specifically by the mesoderm coordinates multiple cellular behaviors in the anterior DPW requisite for the elongation of the cardiac outflow tract and embryonic viability.

38 **Introduction**

39 Congenital heart disease (CHD) is one of the most common birth defects. An estimated
40 40,000 newborns in the U.S. are affected by CHD each year (Tsao et al., 2022).
41 Therefore, it is important to understand the cellular and molecular mechanisms regulating
42 cardiac morphogenesis and the alterations that cause CHD. Several sources of cardiac
43 progenitor cells have been identified (Zhang et al., 2021). Progenitors in the first heart
44 field mainly give rise to the left ventricle, while progenitors in the second heart field (SHF)
45 give rise to the right ventricle, the outflow tract (OFT) and the atria. Correct formation of
46 the OFT is necessary for the proper morphogenesis of the arterial pole of the heart,
47 including intraventricular septation and positioning of the great vessels relative to the
48 cardiac chambers (Cortes et al., 2018). Defects in these processes are among the most
49 common causes of CHD (Tsao et al., 2022). During the initial stages of OFT development,
50 OFT is a single tube connecting the heart with the systemic circulation. In the mouse, the
51 OFT elongates between embryonic day (E) 8.5 and E10.75 of development by the
52 addition of the SHF cells to the nascent heart tube (Meilhac and Buckingham, 2018). The
53 aberrant contribution of SHF cells to the OFT results in defective elongation of the cardiac
54 OFT and aberrant morphogenesis of the arterial pole of the heart.

55

56 Recent findings have shown that SHF cells in the dorsal pericardial wall (DPW) directly
57 behind the forming heart are exquisitely organized and exhibit epithelial properties such
58 as apicobasal polarity (Cortes et al., 2018; Francou et al., 2014). Aberrations in SHF cell
59 polarity and cohesion in the DPW result in shortened OFT and CHD (Cortes et al., 2018;
60 Li and Wang, 2018). For instance, *Tbx1*, a key transcription factor mutated in 22q11

61 deletion syndrome, mediates OFT elongation by regulating SHF cell polarity, organization
62 of the actin cytoskeleton, and epithelial tension in the DPW (Francou et al., 2017; Francou
63 et al., 2014). Similarly, mediators of non-canonical Wnt signaling such as *Vngl2, Wnt5a,*
64 and *Dsh* mediate OFT elongation by regulating apicobasal polarity of SHF cells in the
65 DPW, actin cytoskeleton, and cell intercalation behaviors important for displacing SHF
66 cells from the DPW to join the OFT (Li et al., 2019; Li et al., 2016; Li and Wang, 2018;
67 Ramsbottom et al., 2014; Sinha et al., 2015; Sinha et al., 2012).
68
69 SHF cells in the DPW are regionalized along the anterior-posterior and left-right axes.
70 *Osr1, Hoxb1*, and *Wnt5a* are expressed in the posterior DPW, while *Tbx1* is expressed
71 in the anterior (Stefanovic et al., 2020). We noticed that the expression of the extracellular
72 matrix (ECM) glycoprotein *Fn1* was enriched at the protein and *mRNA* levels in the
73 anterior DPW. In our previous studies using a global deletion of Fn1, we found that cardiac
74 OFTs were short in Fn1-null mutants (Mittal et al., 2013). In addition, the expression of
75 Fn1 or its major receptor integrin $\alpha5\beta1$ in the *Isl1* lineage was required for OFT elongation
76 (Chen et al., 2015), suggesting that Fn1 is an important player in heart development.
77 However, the specific roles of Fn1 in OFT development are not well-understood.
78
79 *Fn1* mRNA is broadly expressed in the paraxial and lateral plate mesoderm of early
80 murine embryos at 1-3 somite stage (Pulina et al., 2011). During heart formation (6-23
81 somites), *Fn1* mRNA continues to be expressed in the splanchnic mesoderm, while its
82 expression in differentiated cardiomyocytes is nearly lost (Mittal et al., 2010). Mesodermal
83 populations expressing *Fn1 mRNA* contain cardiac progenitors, and since heart

84 development is affected in global Fn1-null embryos and embryos with conditional deletion
85 of Fn1, Fn1$^{flox/-}$; Isl1$^{Cre/+}$ (Chen et al., 2015; Mittal et al., 2013), we hypothesized that
86 Fn1 synthesized by cardiac progenitors plays important roles in heart development. To
87 investigate this hypothesis, we used the *Mesp1*$^{Cre/+}$ knock-in strain to ablate Fn1
88 expression conditionally in the anterior mesoderm. In this manuscript, we show that
89 mesodermal Fn1 coordinates multiple cellular behaviors in the DPW necessary for OFT
90 growth by SHF cell accretion from the DPW. The absence of mesodermal Fn1 results in
91 aberrant cellular architecture in the DPW, including defective apicobasal cell polarity,
92 shape, orientation, and mechanotransduction, leading to the shortened OFT and
93 embryonic lethality.
94
95 **Results**
96 **Mesodermal synthesis of Fn1 is required for cardiogenesis and embryonic viability.**
97 The expression of the transcription factor Mesp1 marks the earliest known cardiac
98 progenitors, and the descendants of Mesp1-expressing cells contribute to all mesoderm
99 cells of the heart (Saga et al., 1996; Saga et al., 1999). Therefore, we used the
100 *Mesp1*$^{Cre/+}$ strain to conditionally ablate *Fn1* expression from heart precursors. Although
101 Mendelian proportions of all genotypes were recovered at E9.5, we found that some
102 Fn1$^{flox/-}$; *Mesp1*$^{Cre/+}$ mutant embryos at E9.5 showed mild cardiac defects (S1A-C Fig)
103 and most mutants did not survive past E10.5 (S1D-F Fig). Only 50% of the expected
104 number of Fn1$^{flox/-}$; *Mesp1*$^{Cre/+}$ embryos were recovered at E10.5, and all of the
105 recovered mutants had prominent cardiac edema, defective heart, and were degenerating

106 (S1D-E Fig). No Fn1$^{flox/-}$; *Mesp1*$^{Cre/+}$ mutants were recovered after E13.5 days of
107 gestation (S1F Fig). These data indicated that the expression of *Fn1* in the Mesp1-lineage
108 is important for heart development and embryonic viability.
109
110 **Mesodermal Fn1 regulates the elongation of the cardiac OFT.**
111 The shape of the heart in mutants recovered at E10.5 (S1D-E Fig) suggested that
112 mesodermal Fn1 played a role in the development of the cardiac OFT. To test this
113 hypothesis, we first examined embryos at E8.5 (8-12 somites), when the OFT begins to
114 form. At this stage of development, we did not find alterations in any cardiac structure,
115 and the nascent OFTs in mutants and controls were of similar lengths (S2 Fig). Heart
116 remained similar in shape in control and mutant embryos developed to 18-19 somites,
117 and the sizes of their OFTs were comparable among genotypes (Fig. 1A-D). However,
118 the lengths of the OFTs in mutant embryos isolated at 20-25 somites were significantly
119 shorter than in controls, and both the proximal and the distal portions of the OFTs were
120 affected at this stage (Fig. 1E-H). In control embryos, the right and the left ventricles align
121 in the plane perpendicular to the embryonic anterior-posterior axis (Fig. 1I). In mutants
122 with the shortened OFTs this alignment is distorted (Li et al., 2016) and the right ventricle
123 is shifted anteriorly due to the decreased length of the OFT (Fig. 1J-K). Together, these
124 data indicate that mesodermal Fn1 plays a requisite role in cardiogenesis by regulating
125 the process of OFT elongation.
126
127 **Mesodermal Fn1 regulates epithelial architecture of the second heart field.**

128 Cardiac OFT elongates through the addition of cardiac precursors from SHF cells in the
129 first and second pharyngeal arches and the splanchnic mesoderm of the DPW (Cortes et
130 al., 2018; Li and Wang, 2018; Meilhac and Buckingham, 2018). The length of the OFT
131 remained comparable among controls and mutants by ~19th somite stage of
132 development, suggesting that the addition of SHF cells from the pharyngeal arch
133 mesoderm was not affected by the deletion of mesodermal Fn1 (Meilhac and
134 Buckingham, 2018). The number and proliferation of SHF cells in the splanchnic
135 mesoderm, also known as the dorsal pericardial wall (DPW) were not affected at E8.5
136 (S3 Fig). However, cells in the DPW of E8.5 mutants were disorganized (Fig. 2). Instead
137 of a single layer of epithelial-like cells in Fn1$^{flox/+}$; *Mesp1*$^{Cre/+}$ controls, cells in the
138 anterior DPW of Fn1$^{flox/-}$; *Mesp1*$^{Cre/+}$ mutants were multilayered (compare Fig. 2A-A1
139 with Fig. 2E-E1). In controls, ellipsoid cells were regularly oriented with the longest axis
140 positioned in the ventral-dorsal direction and neatly stacked along the length of the DPW
141 (Fig. 2A-D). Defective cellular architecture was specific to the anterior DPW in the
142 mutants, as cells in the posterior DPW were organized and shaped similar to controls
143 (compare Fig. 2A2 with Fig.2E2, and Fig. 2C with Fig. 2G). Moreover, cells in the anterior
144 DPW of the mutants appeared to be more spherical than in controls (compare Fig. 2A1
145 with 2E1, 2B with 2F, and 2D with 2H).
146
147 To quantify differences in cell shape in 2D and 3D, we measured cell circularity and
148 ellipticity in controls and mutants (Fig. 2I-L). Circularity is a ratio of cell width to cell length.
149 Elongated cells have circularity indexes that deviate from 1, while cuboid or spherical cells

150 have circularity indexes close to 1. Differences in the circularity indexes among SHF cells
151 in the anterior DPW of Fn1$^{flox/+}$; *Mesp1*$^{Cre/+}$ control and Fn1$^{flox/-}$; *Mesp1*$^{Cre/+}$ mutant
152 embryos were statistically significant (Fig. 2I), indicating that control SHF cells were more
153 elongated compared with SHF cells in the mutants. However, no such differences in
154 circularity were observed in the posterior DPW between controls and mutants (Fig. 2J).
155 To determine if 3D cell shape was also affected in the mutants, we segmented individual
156 SHF cells in the anterior DPW and measured ellipticity. Ellipticity was higher in control
157 embryos than in mutants, indicating that in the absence of mesodermal Fn1, SHF cells
158 were more spherical than in controls (Fig 2K). The volume of individual SHF cells was not
159 affected in the mutants (Fig. 2L). These differences in 2D and 3D cell shape were
160 observed at E8.5 and preceded the shortening of the cardiac OFT. There were no
161 differences in cell proliferation at this stage (S3 Fig). The aberrant epithelial architecture
162 of the anterior DPW could also be seen at E9.5 when the elongation of the cardiac OFT
163 becomes detectable in the mutants (S4 Fig). Together, these data suggest that alterations
164 in SHF cell shape in the anterior DPW give rise to defective OFT elongation in the
165 mutants.
166

167 **Mesodermal Fn1 regulates SHF cell orientation and apicobasal polarity in the**
168 **anterior DPW.**

169 To determine mechanisms by which mesodermal Fn1 regulates cellular architecture of
170 the DPW, we tested the hypothesis that Fn1 was important for apicobasal cell polarity. At
171 E8.5, the Golgi apparatus is positioned toward the apical cell surface in SHF cells along
172 the entire length of the DPW (Fig. 3A-A2). However, in the mutants, the orientation of the

173 Golgi apparatus was disorganized, and in some cells the Golgi apparatus faced the basal
174 side in the anterior DPW cells (Fig. 3B-B1), while in the posterior DPW, Golgi were
175 positioned toward the apical side of the cells in controls and mutants alike (compare Fig.
176 3B2 with 3A2, quantified in 3C-G).
177
178 Similar to disorganized Golgi orientation, markers of the apical cell surface were re-
179 distributed in the mutants and were also present at the basal cell surface of SHF cells in
180 the anterior DPW (Fig. 4). These proteins included podocalyxin (Fig. 4A-D) and atypical
181 PKC ζ (aPKC ζ) (compare Fig. 4E-F with Fig. 4H-E, quantified in Fig. 4K). Basal-specific
182 cell properties were not as distorted as apical in the mutants: the expression of laminin γ1
183 was disorganized only in 1 of 3 E8.5 mutants (Fig. 4G, J) and basal cellular protrusions
184 were present on SHF cells in controls and mutants at E9.5 (S5A-C). These studies
185 suggest the expansion of the apical surface of SHF cells in the anterior DPW, while the
186 basal surface was specified. Changes in apical cell polarity were observed at E8.5 before
187 defects in the OFT elongation were detectable. Altogether, these data show that changes
188 in SHF cell shape and polarity within the anterior DWP preceded changes in the OFT
189 elongation and were the likely causes of defective OFT elongation in the mutants (Cortes
190 et al., 2018; Li and Wang, 2018).
191
192 **Mesodermal Fn1 regulates cell cohesion in the SHF and collective cell migration.**
193 Adherence junctions form between the apical and basal cell surfaces (Nelson, 2003).
194 Therefore, we examined the localization of N-Cadherin in the DPW and found that N-
195 cadherin levels were downregulated in the DPW of the mutants (Fig. 5A-D1). To quantify

196 these changes, we used mouse embryo fibroblasts (MEFs) as a model system to
197 determine levels of N-Cadherin protein present on the cell surface of $Fn1^{flox/-}$ (Fn1-
198 heterozygous) and $Fn1^{\Delta/-}$ (Fn1-null) MEFs (generated as in S6 Fig, and Methods).
199 Immunofluorescence and quantitative western blot analysis showed that total and cell-
200 surface levels of N-Cadherin were downregulated in Fn1-null MEFs (Fig. 5E-K).
201 Downregulation of N-Cadherin in the cardiac progenitors within the anterior DPW causes
202 their precautious differentiation (Soh et al., 2014). Consistent with these findings, we
203 observed expanded expression of sarcomeric myosin heavy chain (assayed by the MF-
204 20 antibody) in the anterior DPW of our mutants (S7 Fig).
205
206 Cell cohesion is important for the collective cell migration (Friedl and Mayor, 2017). We
207 hypothesize that disrupted expression of N-cadherin in our mutants interfered with the
208 collective cell migration of cardiac precursors joining the OFT. Since N-Cadherin was
209 downregulated in Fn1-null MEFs (Fig. 5E-K), we used this model to determine whether
210 the synthesis of Fn1 by MEFs was important for their collective cell migration. For this
211 experiment, we generated four lines of MEFs (S6 Fig): 1) $Fn1^{flox/+}$ MEFs expressing wild-
212 type levels of Fn1, 2) $Fn1^{flox/-}$ MEFs (in these MEFs, the floxed Fn1 allele expresses
213 Fn1, and "-" Fn1 allele is a null allele), 3) $Fn1^{\Delta/+}$ MEFs in which the floxed region of Fn1
214 allele was deleted generating an Fn1-null allele (Δ) (Sakai et al., 2001), and 4) $Fn1^{\Delta/-}$
215 MEFs, which are Fn1-null (S6D-E Fig). Monolayer scratch assay showed that scratch
216 wounds made in $Fn1^{\Delta/-}$ MEF monolayers closed slower than in $Fn1^{flox/+}$, $Fn1^{flox/-}$, or in

217 $Fn1^{\Delta/+}$ MEFs (S8 Fig). The speed of collective cell migration of $Fn1^{\Delta/-}$ MEFs was slower
218 than in control MEFs (Fig. 6A-E). Remarkably, $Fn1^{flox/-}$ and $Fn1^{\Delta/+}$ MEFs carrying one
219 Fn1-null allele (- or Δ) and expressing about 50% less Fn1 than $Fn1^{flox/+}$ cells (S6D-E
220 Fig) showed a significant reduction in the speed of collective cell migration compared with
221 $Fn1^{flox/+}$ cells carrying two alleles of Fn1 (S6 Fig; Fig. 6E). This finding indicated the dose-
222 dependent requirement for Fn1 in collective cell migration. When MEFs were plated
223 sparsely, migration of single cells was comparable between control and mutant MEFs
224 (Fig. 6F-H). These data indicate that synthesis of Fn1 by MEFs regulates the speed of
225 collective cell migrating but not the speed of cells migrating individually. We then
226 explanted pharyngeal mesoderm from E8.5 embryos and measured the speed of
227 collective cell migration in explants from $Fn1^{flox/+}$; *Mesp1*$^{Cre/+}$ control and $Fn1^{flox/-}$;
228 *Mesp1*$^{Cre/+}$ mutant embryos (Fig. 6I-K). We observed decreased collective cell migration
229 in four of six embryos (Fig. 6K). Together, these studies suggest that mesodermal Fn1
230 regulates collective cell migration of SHF cells to facilitate the elongating cardiac OFT.
231

232 **Mesodermal Fn1 regulates mechanotransduction in the second heart field.**

233 Mechanical tension in the DPW is important for the OFT elongation (Francou et al., 2017).
234 It is mediated by the nuclear localization and activity of the transcription factor YAP, a
235 central transducer of the mechanical signals (Francou et al., 2017). Defective cell shape
236 and orientation of SHF cells in the anterior DPW of $Fn1^{flox/-}$; *Mesp1*$^{Cre/+}$ mutants
237 suggested that mutant SHF cells are deficient in generating, sensing, or responding to

238 mechanical cues. The remodeling of the actin cytoskeleton, nuclear localization of YAP,
239 and the expression of YAP's direct transcriptional target *CTGF* are modulated by the
240 mechanical properties of the tissue microenvironment (Dupont, 2016). Remodeling of
241 actin cytoskeleton and nuclear localization of YAP are known to be facilitated by cell
242 adhesion to Fn1 *in vitro* (Kim and Gumbiner, 2015; Singh et al., 2010). To test whether
243 mesodermal Fn1 was required for cytoskeletal remodeling and signaling by YAP in the
244 DPW, we first stained control and Fn1$^{flox/-}$; *Mesp1*$^{Cre/+}$ mutant embryos to detect
245 filamentous (F)-actin. We found that F-actin organization at E9.5 was disrupted
246 specifically in the anterior DPW of the mutants (Fig. 7): F-actin filaments were shorter and
247 their orientation was disorganized (Fig. 7). The length and orientation of F-actin in the
248 posterior and middle DPW were comparable between genotypes (S9 Fig). These
249 changes were concordant with altered YAP localization in the anterior DPW of mutants
250 (Fig. 8, compare Fig. 8A1 with 8B1, quantified in Fig. 8C). Nuclear localization of YAP in
251 the posterior DPW was not affected (Fig. 8A2, B2, and Fig. 8D). In the nucleus, YAP acts
252 as a transcriptional co-activator, and *CTGF* is one of the direct transcriptional targets of
253 YAP. We found that the expression of *CTGF* is enriched in the anterior DPW of controls
254 (Fig. 8E-I). Consistent with the defective localization of YAP in the anterior DPW, the
255 expression of *CTGF mRNA* was downregulated in the anterior DPW of Fn1$^{flox/-}$;
256 *Mesp1*$^{Cre/+}$ mutants. YAP signaling also regulates SHF cell proliferation in the DPW at
257 E9.5, and concordantly, we found that cell proliferation in DPW and the OFT was
258 decreased in the mutants relative to controls (S3D-F, Fig; S10 Fig). Cell survival,
259 measured by the TUNEL assay was not affected in the mutants at E9.5 (S3M-N1; S11

260 Fig). Together, these data indicate an essential role of mesodermal Fn1 in
261 mechanotransduction within the anterior DPW.
262
263 **Cell type-specific source of Fn1 mRNA and protein in the pharynx**
264 *Fn1 mRNA* and protein are dynamically and non-uniformly expressed in developing
265 embryos (Chen et al., 2015; Mittal et al., 2010), and previous studies in our lab and others
266 demonstrated requisite, cell type-specific functions of Fn1 during embryonic
267 development, angiogenesis, and cell migration (Cseh et al., 2010; Turner et al., 2017;
268 Wang and Astrof, 2016; Zimmerman et al., 2017). SHF cells in the DPW and cells in the
269 pharyngeal endoderm are closely apposed in early embryos, and *Fn1* mRNA is
270 synthesized by both tissues (Fig. 9A-B1). We found that *Fn1* mRNA and protein levels
271 were enriched nearly 2-fold in the anterior relative to the posterior DPW (Fig. 9G-I). In the
272 anterior, the level of *Fn1 mRNA* expression in the SHF was about 2-fold higher than in
273 the anterior endoderm (Fig. 9G, WT column). In contrast, in the posterior DPW, *Fn1*
274 *mRNA* levels in the SHF and the endoderm were comparable (Fig. 9H, WT column). In
275 $Fn1^{flox/+}$; $Mesp1^{Cre/+}$ embryos that serve as controls for the majority of our experiments,
276 one allele of Fn1 is deleted in the mesoderm, leading to ~50% decrease in the level of
277 *Fn1 mRNA* synthesized by the SHF relative to wild-type embryos (Fig. 9C-D1, and 9G-
278 H, CTRL columns). In $Fn1^{flox/-}$; $Mesp1^{Cre/+}$ mutants, levels of *Fn1* mRNA in the SHF
279 were undetectable (Fig. 9E-F1). However, *Fn1 mRNA* remained synthesized by the
280 endoderm (Fig. 9E-F1). The loss of *Fn1 mRNA* in the mesoderm but not in the endoderm
281 is consistent with the known specificity of Cre expression in the $Mesp1^{Cre/+}$ strain (Saga

282 et al., 1996; Saga et al., 1999). This experiment also shows that *Fn1 mRNA* is efficiently
283 downregulated in the SHF.
284
285 In the heart at E9.5, Fn1 is nearly exclusively synthesized by the endocardium (Chen et
286 al., 2015; Ffrench-Constant and Hynes, 1988; Suzuki et al., 1995), and we found a near
287 complete loss of Fn1 protein in the left ventricle of the mutants (compare Fig. 9J-J1 with
288 Fig. 9K-K1, quantified in Fig. 9O). These studies demonstrate that Fn1 protein is
289 downregulated in Mesp1-derived cells in Fn1$^{flox/-}$; *Mesp1*$^{Cre/+}$ embryos.
290
291 **Mesodermal Fn1 is the essential source of Fn1 in the anterior DPW.**
292 Investigation of *Fn1 mRNA* and protein expression demonstrated that *Fn1 mRNA* is
293 synthesized by the pharyngeal endoderm in Fn1$^{flox/-}$; *Mesp1*$^{Cre/+}$ mutants and that Fn1
294 protein is present at the endoderm-SHF interface of the mutants and controls alike
295 (compare Fig. 9J2-J3 with Fig. K2-K3, quantified in 9L-N). Quantitative analyses of
296 immunofluorescence show that the difference in Fn1 protein expression between the
297 anterior and posterior DPW is steeper in the mutants (Fig. 9L-L1). Importantly, the level
298 of Fn1 protein in the anterior DPW is not significantly different between Fn1$^{flox/+}$;
299 *Mesp1*$^{Cre/+}$ controls and Fn1$^{flox/-}$; *Mesp1*$^{Cre/+}$mutants (Fig. 9M).
300
301 Despite the presence of comparable levels of Fn1 protein in the anterior DPW of Fn1$^{flox/+}$;
302 *Mesp1*$^{Cre/+}$control and Fn1$^{flox/-}$; *Mesp1*$^{Cre/+}$mutant embryos, the epithelial organization

303 of the anterior DPW was disrupted in the mutants resulting in a shortened OFT. This
304 experiment suggested that SHF-derived Fn1 functions cell-autonomously. To test the cell-
305 autonomous requirement of Fn1 and rule out the possibility that differences Fn1 protein
306 levels contributed to defects in the DPW and OFT elongation in Fn1$^{flox/-}$;
307 *Mesp1*$^{Cre/+}$mutants, we deleted Fn1 using *Sox17*$^{2A\text{-}iCre/+}$strain, in which Cre
308 recombinase is expressed in the endoderm and endothelium (Engert et al., 2009). In
309 Fn1$^{flox/-}$; *Sox17*$^{2A\text{-}iCre/+}$mutants, *Fn1 mRNA* is downregulated in the endoderm but it is
310 still synthesized by the SHF cells of the DPW (S12A-A1 Fig). And although the levels of
311 Fn1 protein underlying the DPW were substantially reduced in Fn1$^{flox/-}$; *Sox17*$^{2A\text{-}}$
312 $^{iCre/+}$mutants (S12B-B1 Fig), the epithelial organization and the expression of N-cadherin
313 were not affected (S12C-C1 Fig). Together, these data indicate 1) that the presence of
314 Fn1 protein synthesized by the endoderm is not sufficient to rescue the absence of
315 mesodermal Fn1 synthesized in the SHF and 2) that synthesis of Fn1 by the SHF is
316 specifically required for the proper cellular architecture and mechanotransduction in the
317 anterior DPW and consequently for the OFT elongation and embryonic viability.
318

319 **Conclusion**

320 Distinct gene programs regulate cell behaviors in the anterior and the posterior DPW
321 important for OFT elongation and proper development of the arterial pole of the heart (Li
322 and Wang, 2018; Stefanovic et al., 2020). We found that *Fn1* mRNA and protein are
323 enriched in SHF cells within the anterior DPW and that the expression of *Fn1* specifically

324 in the SHF coordinates multiple cellular behaviors necessary for the accretion of SHF
325 cells in the elongating OFT (Fig. 10).
326
327 **Discussion**
328 In this manuscript, we show that Fn1 synthesized by the mesoderm is required for the
329 proper cell shape, cell polarity, cell orientation, and the orderly stacking of SHF cells in
330 the anterior DPW at E8.5. In Fn1$^{flox/-}$; *Mesp1*$^{Cre/+}$mutants, defects in these properties
331 occur prior to the observable deficiencies in the OFT elongation, indicating that defects in
332 DPW architecture cause aberrant OFT elongation in Fn1$^{flox/-}$; *Mesp1*$^{Cre/+}$mutants.
333
334 Transient genetic labeling of SHF cells at the earliest time of their emergence during
335 gastrulation with the aid of Mesp1 $^{Cre/+}$ and Rosa-Confetti strains showed clusters of SHF
336 cells in the DPW (Francou et al., 2017) supporting the idea that OFT elongation occurs
337 through the collective cell migration of SHF cells from the DPW to join the OFT. We found
338 that SHF-derived Fn1 is important for regulating cell cohesion in the SHF by mediating
339 the expression of N-cadherin and, consequently, for the collective cell migration.
340
341 Fn1 is enriched in the anterior DPW and synthesis of Fn1 by the SHF is required for the
342 proper epithelial organization of the anterior DPW. Fn1 synthesized by SHF cells
343 regulates cell shape, orientation, and apicobasal polarity, as well as SHF cell
344 differentiation, proliferation, and mechanotransduction. Thus, Fn1 is a central player

345 responsible for coordinating multiple cellular behaviors regulating the morphogenesis of
346 the cardiac OFT.
347
348

349 **Materials and Methods**

350 *Antibodies:*

351 See Supplemental Table 1 for all antibody information.

352

353 *Mouse strains:*

354 All experiments involving vertebrate animals were approved by the Rutgers University
355 Institutional Animal Care and Use Committee and were performed following federal
356 guidelines for the humane care of animals. C57BL/6J mice (cat # 0664) and
357 Rosa$^{mTmG/mTmG}$ mice, Gt(ROSA)26Sor$^{tm4(ACTB-tdTomato,-EGFP)Luo}$ mice (Cat# 037456)
358 (Muzumdar et al., 2007), were purchased from Jackson Laboratories. Fn1$^{flox/flox}$ mice were
359 a gift from Reinhardt Fassler (Sakai et al., 2001). Mesp1$^{Cre/+}$ knock-in mice (Saga et al.,
360 1996; Saga et al., 1999) were obtained from Dr. Yumiko Saga. Fn1$^{+/-}$ strain (George et
361 al., 1997; George et al., 1993) was a gift from Richard Hynes. Sox17$^{2A-iCre}$ mice were a
362 gift from Heicko Lickert (Engert et al., 2009). For experiments, Fn1$^{+/-}$ mice were crossed
363 with Mesp1$^{Cre/+}$ knock-in mice to generate Fn1$^{+/-}$; Mesp1$^{Cre/+}$ males which were
364 propagated by mating with C57BL/6J females. To obtain embryos, Fn1$^{+/-}$; Mesp1$^{Cre/+}$
365 males were crossed with Fn1$^{flox/flox}$; Rosa$^{mTmG/mTmG}$ females, and pregnant females were
366 dissected at days specified in the figures. Mice and embryos were genotyped according

367 to published protocols (Engert et al., 2009; George et al., 1993; Saga et al., 1999).
368 Embryos were staged by counting somites.
369
370 *Cell culture and generation of cell lines:*
371 Mouse embryo fibroblasts (MEFs) were isolated from E13.5 embryos resulting from the
372 mating of $Fn1^{+/-}$ mice with $Fn1^{flox/flox}$; $ROSA^{mTmG/mTmG}$ mice.
373 MEFs were cultured on plates pre-coated with 0.1% gelatin (Sigma, #G1890) dissolved
374 in H_2O and maintained in complete medium, which consisted of Dulbecco's Modified
375 Eagle's medium (DMEM) with 4.5 g/L glucose, L-glutamine & sodium pyruvate (Corning,
376 #10-013-CM) supplemented with 100 U/ml penicillin, 100 μg/ml streptomycin (Gibco,
377 #15140-122), 1% v/v GlutaMax (L-glutamin, Gibco, #35050061) and 10% v/v fetal bovine
378 serum (FBS, Gemini Biosciences, #100-106) in a humidified incubator with 5% CO_2 at
379 37°C.
380
381 To generate MEFs lacking Fn1 (Fn1-null), or control, Fn1-heterozygous (Fn1-het) MEFs,
382 $Fn1^{flox/+}$; $ROSA^{mTmG/+}$ and $Fn1^{flox/-}$; $ROSA^{mTmG/+}$ MEFs were infected with
383 adenoviruses encoding Cre recombinase, Ad-Cre-IRED-GFP (Vector Biolabs, #1710).
384 Cre-induced recombination not only leads to the ablation of Fn1 by recombining the floxed
385 Fn1 sequence but also induces the expression of membrane-tethered GFP in these cells.
386 For this experiment, $3x10^4$ MEFs were plated on gelatin-coated wells of 6-well plates. 24
387 hours later, cells were rinsed twice with Phosphate Buffered Saline 1X Sterile Solution
388 (PBS, RPI Research Products, # P10400-500) and infected with Cre adenovirus diluted
389 to the multiplicity of infection of 500 in DMEM without FBS. 20 hours post-infection, the

390 medium was replaced by the complete medium. Although each of these cell types carries
391 one ROSA^{mTmG} allele, only cells infected with Ad-Cre are constitutively and permanently
392 marked by the expression of GFP due to the recombination of the reporter locus. GFP
393 expression from the adenovirus is transient and dissipates after three days post-infection.
394 After expansion, Ad-Cre-treated cells were sorted to generate Fn1$^{\Delta/-}$ (Fn1-null, GFP+),
395 Fn1$^{flox/-}$ (Fn1-heterozygous, GFP-), Fn1$^{\Delta/+}$ (Fn1-heterozygous, GFP+), and Fn1$^{flox/+}$ (Fn1-
396 wild type, GFP-) MEF lines. Western blot analysis was used to assay Fn1 expression.
397
398 *MEF protein lysates:*
399 Cells were plated in 6-well dishes at a density of 2×10^5 cells per well. After 48 hours, cells
400 were washed twice with cold PBS supplemented with 0.1 mM $CaCl_2$ and 1 mM
401 $MgCl_2$ (PBS-Ca^{2+}/Mg^{2+}) and lysed with 400 μl of RIPA lysis buffer (50 mM Tris-Cl, 150
402 mM NaCl, 2 mM EDTA, 1% v/v NP-40, 0.5% w/v sodium deoxycholate, 0.1% w/v SDS,
403 1X protease inhibitor cocktail (Cell Signaling Technology, #5871), pH 8.0).
404 The samples were centrifuged at 16,000 × g for 15 min at 4°C.
405 Protein concentration was determined using BCA protein assay (Pierce™ BCA Protein
406 Assay Kit, #23225). Then, lysis buffer was added to equalize protein concentration across
407 samples. 4xNuPAGE™ LDS Sample buffer (Thermo Scientific, #NP0008) with 10% β-
408 mercaptoethanol (Sigma, #63689) was added to each sample to the final concentration
409 of 1X NuPAGE and 2.5% β-mercaptoethanol. Samples were heated to 95°C for 5 minutes
410 prior to loading on gels.
411
412 *Immunoblotting and densitometry quantification:*

413 For immunoblotting, samples were resolved using 4-12% Tris-Glycine gel (Invitrogen,
414 #XP04120BOX) at 130 V in 1x Tris-Glycine SDS Running Buffer (Invitrogen, # LC2675)
415 for 1 hour 30 minutes. Proteins were then transferred to nitrocellulose membranes with a
416 0.2 µm pore size (Bio-Rad, # 1620122) and 1x Tris-Glycine, 15% methanol transfers
417 buffer (10x Tris-Glycine buffer: 30g Tris Base. 144 g Glycine in 1L of ddH20, pH: 8.5).
418 The transfer was carried out at 90 V for 2 hours in ice.
419 After the transfer, the nitrocellulose membranes were blocked with Intercept Blocking
420 Buffer (Li-Cor, # 927-60001) for 1 hour. Primary antibodies were diluted in Intercept
421 Antibody Diluent (Li-Cor, # 927-65001) and incubated overnight at 4°C. After 24h, the
422 nitrocellulose membranes were washed three times with PBS containing 0.1% Tween for
423 10 min. We used IRDye 680RD Donkey anti-Rabbit IgG (#926-68073), and IRDye
424 800CW Donkey anti-Mouse IgG Secondary Antibody (#926-32212) as secondary
425 antibodies in a 1:15000 dilution in Intercept Antibody Diluent (Li-Cor, # 927-65001). The
426 nitrocellulose membranes were incubated with the secondary antibodies for 1 hour at
427 room temperature. Finally, membranes were washed three times with PBS 0.1% Tween
428 for 10 minutes and imaged using Li-Cor Odyssey 9120 Gel Imaging System (#ODY-
429 2425). The density of unsaturated pixels was determined using ImageJ software (version
430 2.1.0/1.53c4). For each condition, protein bands were quantified from at least three
431 independent experiments.
432
433 *Cell surface biotinylation:*
434 $3.5x10^5$ cells were plated on gelatin-coated 10 cm plates. After 48 hours of growth, cells
435 were washed twice with ice-cold PBS supplemented with 0.1 mM $CaCl_2$ and 1 mM $MgCl_2$

436 (PBS-Ca^{2+}/Mg^{2+}), followed by incubation with 1 mM EZ-Link Sulfo-NHS-LC-Biotin
437 (Thermo Scientific, #21335) in PBS-Ca^{2+}/Mg^{2+} for 30 min at 4°C. The biotinylation
438 reaction was quenched by incubating cells with Tris-buffered solution (50 mM Tris-HCl,
439 pH 7.4) for 10 min at 4°C. After two subsequent washes with PBS-Ca^{2+}/Mg^{2+}, cells were
440 lysed with 600 μl of RIPA lysis buffer (50 mM Tris-Cl, 150 mM NaCl, 2 mM EDTA, 1% v/v
441 NP-40, 0.5% w/v sodium deoxycholate, 0.1% w/v SDS, 1X protease inhibitor cocktail (Cell
442 Signaling Technology, #5871), pH 8.0). To remove insoluble material, cell extracts were
443 clarified by centrifugation at 16,000 x g for 15 min at 4°C, and soluble biotinylated protein
444 concentration was determined using BCA protein assay (Pierce™ BCA Protein Assay Kit,
445 #23225). 300 μg of protein per sample was incubated with 40 μl of Neutravidin-Agarose
446 beads (Thermo Scientific, # 29202) pre-washed with RIPA lysis buffer. After 1 hour of
447 incubation at 4°C, the Neutravidin-Agarose beads were washed 3 times with RIPA lysis
448 buffer containing 1X protease inhibitor cocktail. 120 μl of 1X NuPAGE™ LDS Sample
449 buffer (Thermo Scientific, #NP0008) with 2.5% β-mercaptoethanol (Sigma, #63689) and
450 1X protease inhibitor cocktail was added to beads and resolved by SDS-PAGE (Arriagada
451 et al., 2020).
452
453 *Immunofluorescence microscopy:*
454 $2x10^4$ cells were plated on gelatin-coated #1.5 round glass coverslips (Fisher Scientific,
455 t#12-545-81) in 24-well dishes. After for 48 hours, cells were washed with PBS that was
456 pre-warmed to 37°C for 5 minutes and fixed with 4% PFA (Fisher Scientific # 50-980-487,
457 diluted in PBS) for 20 minutes at room temperature. Then, cells were washed three times
458 with PBS for 5 minutes each and permeabilized with PBS containing 0.1% Triton-X 100

459 (PBST) for 15 minutes. Cells were blocked with 5% Donkey serum (Sigma, #d9663) in
460 PBST (blocking solution) for 30 minutes. After blocking, cells were incubated with the
461 primary antibodies diluted in blocking solution overnight at 4◦C. Following 3 washes in
462 PBST for 10 minutes each, cells were incubated with secondary antibodies diluted in
463 blocking solution for 60 minutes at room temperature. Finally, cells were washed three
464 times with PBST for 10 minutes, mounted using a 50% v/v Glycerol, 50% v/v Methanol
465 solution.
466
467 *Migration assay:*
468 $1x10^4$ cells were plated on gelatin-coated 8-well ibidi dishes (Ibidi, #80827) for 72 hours.
469 When cells were confluent, the monolayer was scratched with a sterile 10 µl pipette tip.
470 Cell debris was washed out with PBS, and incubated with imaging medium 100 µl
471 FluoroBrite DMEM (Thermo Fisher Scientific, #A1896701) supplemented with 100 U/ml
472 penicillin, 100 µg/ml streptomycin (Gibco, #15140-122), 1% v/v GlutaMax (L-glutamin,
473 Gibco, #35050061) and 2% v/v fetal bovine serum (FBS, Gemini Biosciences, #100-106).
474 Images were acquired every 5-min for 14 hours with a Nikon A1-HD25 565 inverted
475 confocal microscope equipped with the DUG 4-Channel Detector and 2 GaAsP, 2 high
476 566 sensitivity PMTs, and a motorized XYZ stage with Nikon's Perfect Focus 4 system.
477 Plan Fluor 567 40x Oil (numerical aperture 1.3, # MRH01401) immersion objective was
478 used for live imaging. The movement of cells from every 10th frame was manually tracked
479 using the plug-in Manual Tracking developed for ImageJ
480 (http://rsb.info.nih.gov/ij/plugins/track/track.html). Speed, directionality and trajectory plot
481 were performed as previously described (Gorelik and Gautreau, 2014).

482

483 *Whole Mount Immunofluorescence staining:*

484 Timed matings were set up to obtain embryos at specific embryonic stages. Vaginal plugs
485 were checked daily, and noon of the day the plug was found was considered to be an
486 embryonic day (E) 0.5 of gestation. Embryo dissections were aided by the use of Zeiss
487 Stemi 2000C stereomicroscope. Embryos were dissected into ice-cold PBS, yolk sacs
488 were kept for genotyping. After dissection, embryos were fixed with 4% PFA overnight at
489 4°C. Then, embryos were washed two times with ice-cold PBS and permeabilized with
490 PBS containing 0.1% Triton- X 100 (PBST) overnight at 4°C. Embryos were blocked with
491 10% Donkey serum in PBST (blocking solution) overnight at 4°C. After blocking, embryos
492 were incubated with the primary antibodies diluted in blocking solution for 3 days at 4°C.
493 Following four 1 hour-washes with PBST, embryos were incubated with secondary
494 antibodies diluted in blocking solution for 3 days at 4°C. Finally, after four washes with
495 PBST for 1 hour each, embryos were embedded in 1% agarose (Bio-Rad Laboratories,
496 #1613101), and cleared using methanol and Benzyl Alcohol (Sigma, # B-1042)/ Benzyl
497 Benzoate (Sigma, #B-6630) as described (Ramirez and Astrof, 2020). For imaging,
498 embryos were a placed between two #1.5 coverslips (VWR, #16004-312) separated by a
499 rubber spacer (Grace Bio Labs, # 664113).

500

501 *Whole Mount Immunofluorescence in situ hybridization:* After dissection, embryos were
502 fixed with 4% PFA overnight at 4°C and washed twice with PBS. *In situ hybridization*
503 assay carried out using the RNAscope® Multiplex Fluorescent v2 reagents (Advanced

504 Cell Diagnostics, # 323110) as previously described (Nomaru et al., 2021). We used a
505 C1 probe for Fn1 (#408181) and C2 probe for CTGF (#314541-C2)
506
507 *Embryo Cryosection and immunofluorescence staining:*
508 After dissection, embryos were fixed with 4% PFA overnight at 4°C and washed twice
509 with PBS. Embryos were then incubated with 10% sucrose in PBS for 4 hours at room
510 temperature and then with 20% sucrose in PBS overnight at 4°C with agitation. Embryos
511 were then incubated with 30% sucrose in PBS for 4 hours at room temperature, and then
512 with a 1:1 mixture of Tissue-Tek O.C.T. Compound (O.C.T, Sakura, #4583) and 30%
513 sucrose solution for 1 hour at room temperature with agitation. Finally, embryos were
514 placed into 100% O.C.T for 10-20 minutes without agitation. Embryos were then
515 positioned in fresh 100% OCT solution in plastic molds and frozen by dipping the mold
516 into 2-methyl butane chilled on dry ice. 8 µm-thick sections were obtained using a Leica
517 CM1950 Cryostat. For long term storage, slides were kept at -80ºC. For
518 immunofluorescence, we used an ImmEdge Hydrophobic Pen (VWR, 101098-065) to
519 draw a hydrophobic barrier around tissue sections. Tissue sections were permeabilized
520 by washing with PBS containing 0.05% Tween-20 (Sigma, cat # P7949) 3 times for 5
521 minutes. Then, slides were placed in a humidified chamber, and sections were incubated
522 with a blocking buffer containing 5% donkey serum in PBS-0.05% Tween for 30 minutes
523 at room temperature. The blocking buffer was then removed and replaced with primary
524 antibodies diluted in blocking buffer, and incubated with sections overnight at 4°C. After
525 washing the slides 3 times for 5 minutes with PBS-0.05% Tween, sections were incubated
526 with secondary antibodies for 1 hour at room temperature. Finally, slices were washed 3

527 times for 5 minutes each with PBS-0.05%Tween and mounted using a 50% v/v Glycerol,
528 50% v/v Methanol solution. Sections stained with SiR-Actin (Cytoskeleton, #CY-SC001,
529 2μM), samples were mounted with Vectashield Antifade Mounting Medium (Vector
530 laboratories, #H-1000).
531
532 *TUNEL assay:*
533 TUNEL assay was performed using the In Situ Cell Death Detection Kit from Roche (cat
534 #11684795910) following manufacturer's instructions.
535
536 *Imaging, quantifications, and statistical analyses:*
537 Embryos were imaged using confocal microscopy using Nikon A1R microscope with 20x
538 CFI Apo LWD Lambda S water immersion objective (#MRD77200) or 25x CFI Plan Apo
539 Lambda S silicone oil objectives (#MRD73250). Cultured cells were imaged using
540 confocal microscopy and the Plan Fluor 567 40x Oil immersion objective (numerical
541 aperture 1.3, # MRH01401). 3D reconstructions, surfacing, and quantifications were
542 performed using IMARIS software (Bitplane, USA). Fluorescence intensity and angles
543 were measured using Fiji software and plotted using Orient software, version 3.1.1. Cell
544 ellipticity was measured using Imaris as described (Andrews et al., 2021). Statistical
545 analyses were performed using Prism 9, version 9.4.1 (GraphPad Software, LLC).
546
547 *Explant assay:*
548 Embryos were dissected at E8.5 in cold sterile PBS. The head, heart and tissues posterior
549 to the heart were removed, and the pharyngeal region was placed in a well of 8-well Ibidi

550 plates pre-coated with 150 µg/mL of Collagen-I working solution (11.6 µL glacial acetic
551 acid, 10 ml of sterile ddH2O and 163.4 µl of Collagen I Concentrate (9.18 mg/ml) (Corning,
552 #354249) as described in (Wang and Astrof, 2016; Wang and Astrof, 2017). For the first
553 24 hours, the explant was cultured in the presence of 20 µl of DMEM/F12 medium (Gibco,
554 11320-033) containing 100 U/ml penicillin, 100 µg/ml streptomycin (Gibco, #15140-122),
555 and 10% v/v fetal bovine serum (FBS, Gemini Biosciences, #100-106) in a humidified
556 incubator with 5% CO2 at 37°C. After the explants were attached, the imaging medium
557 was added, and the explants were filmed for 14 hours, as described above.
558
559 *Embryo protein extract:*
560 Embryos were lysed with 100 µL of SDS lysis buffer (0.1 M Tris-HCl, 0.2% SDS, 5mM
561 EDTA pH 8 containing 1X protease inhibitor cocktail and homogenized by drawing the
562 lysates 10 times though a 27G syringe. 33.3 µl of 4X NuPAGE™ LDS Sample buffer
563 containing 10% β-mercaptoethanol were added to each sample, samples were incubated
564 at 95°C for 5 minutes.
565
566
567
568 **Acknowledgements:** We thank Sam Russo for help with mouse colony maintenance and
569 genotyping. These studies are supported by the American Heart Association Postdoctoral
570 Fellowship to CA, grant # 836254, and by the National Heart, Lung, and Blood Institute of the
571 National Institutes of Health (R01 HL103920, R01 HL134935 and R01 HL158049) to SA.
572

Figure Legends

Each figure legend is displayed next to the figure.

576 **Literature Cited**

577 Andrews, T.G.R., W. Ponisch, E.K. Paluch, B.J. Steventon, and E. Benito-Gutierrez.
578 2021. Single-cell morphometrics reveals ancestral principles of notochord development.
579 *Development*. 148.

580 Arriagada, C., V.A. Cavieres, C. Luchsinger, A.E. Gonzalez, V.C. Munoz, J. Cancino, P.V.
581 Burgos, and G.A. Mardones. 2020. GOLPH3 Regulates EGFR in T98G Glioblastoma
582 Cells by Modulating Its Glycosylation and Ubiquitylation. *Int J Mol Sci*. 21.

583 Chen, D., X. Wang, D. Liang, J. Gordon, A. Mittal, N. Manley, K. Degenhardt, and S.
584 Astrof. 2015. Fibronectin signals through integrin alpha5beta1 to regulate cardiovascular
585 development in a cell type-specific manner. *Dev Biol*. 407:195-210.

586 Cortes, C., A. Francou, C. De Bono, and R.G. Kelly. 2018. Epithelial Properties of the
587 Second Heart Field. *Circ Res*. 122:142-154.

588 Cseh, B., S. Fernandez-Sauze, D. Grall, S. Schaub, E. Doma, and E. Van Obberghen-
589 Schilling. 2010. Autocrine fibronectin directs matrix assembly and crosstalk between cell-
590 matrix and cell-cell adhesion in vascular endothelial cells. *J Cell Sci*. 123:3989-3999.

591 Dupont, S. 2016. Role of YAP/TAZ in cell-matrix adhesion-mediated signalling and
592 mechanotransduction. *Exp Cell Res*. 343:42-53.

593 Engert, S., W.P. Liao, I. Burtscher, and H. Lickert. 2009. Sox17-2A-iCre: a knock-in
594 mouse line expressing Cre recombinase in endoderm and vascular endothelial cells.
595 *Genesis*. 47:603-610.

596 Ffrench-Constant, C., and R.O. Hynes. 1988. Patterns of fibronectin gene expression and
597 splicing during cell migration in chicken embryos. *Development*. 104:369-382.

598 Francou, A., C. De Bono, and R.G. Kelly. 2017. Epithelial tension in the second heart field
599 promotes mouse heart tube elongation. *Nat Commun*. 8:14770.

600 Francou, A., E. Saint-Michel, K. Mesbah, and R.G. Kelly. 2014. TBX1 regulates epithelial
601 polarity and dynamic basal filopodia in the second heart field. *Development*. 141:4320-
602 4331.

603 Friedl, P., and R. Mayor. 2017. Tuning Collective Cell Migration by Cell-Cell Junction
604 Regulation. *Cold Spring Harb Perspect Biol*. 9.

605 George, E.L., H.S. Baldwin, and R.O. Hynes. 1997. Fibronectins are essential for heart
606 and blood vessel morphogenesis but are dispensable for initial specification of precursor
607 cells. *Blood*. 90:3073-3081.

608 George, E.L., E.N. Georges-Labouesse, R.S. Patel-King, H. Rayburn, and R.O. Hynes.
609 1993. Defects in mesoderm, neural tube and vascular development in mouse embryos
610 lacking fibronectin. *Development*. 119:1079-1091.

611 Gorelik, R., and A. Gautreau. 2014. Quantitative and unbiased analysis of directional
612 persistence in cell migration. *Nat Protoc*. 9:1931-1943.

613 Kim, N.G., and B.M. Gumbiner. 2015. Adhesion to fibronectin regulates Hippo signaling
614 via the FAK-Src-PI3K pathway. *J Cell Biol*. 210:503-515.

615 Li, D., A. Angermeier, and J. Wang. 2019. Planar cell polarity signaling regulates
616 polarized second heart field morphogenesis to promote both arterial and venous pole
617 septation. *Development*. 146.

618 Li, D., T. Sinha, R. Ajima, H.S. Seo, T.P. Yamaguchi, and J. Wang. 2016. Spatial
619 regulation of cell cohesion by Wnt5a during second heart field progenitor deployment.
620 *Dev Biol*. 412:18-31.

621 Li, D., and J. Wang. 2018. Planar Cell Polarity Signaling in Mammalian Cardiac
622 Morphogenesis. *Pediatr Cardiol*. 39:1052-1062.

623 Meilhac, S.M., and M.E. Buckingham. 2018. The deployment of cell lineages that form
624 the mammalian heart. *Nat Rev Cardiol*. 15:705-724.

625 Mittal, A., M. Pulina, S.Y. Hou, and S. Astrof. 2010. Fibronectin and integrin alpha 5 play
626 essential roles in the development of the cardiac neural crest. *Mech Dev*. 127:472-484.

627 Mittal, A., M. Pulina, S.Y. Hou, and S. Astrof. 2013. Fibronectin and integrin alpha 5 play
628 requisite roles in cardiac morphogenesis. *Dev Biol*. 381:73-82.

629 Muzumdar, M.D., B. Tasic, K. Miyamichi, L. Li, and L. Luo. 2007. A global double-
630 fluorescent Cre reporter mouse. *Genesis*. 45:593-605.

631 Nelson, W.J. 2003. Adaptation of core mechanisms to generate cell polarity. *Nature*.
632 422:766-774.

633 Nomaru, H., Y. Liu, C. De Bono, D. Righelli, A. Cirino, W. Wang, H. Song, S.E. Racedo,
634 A.G. Dantas, L. Zhang, C.L. Cai, C. Angelini, L. Christiaen, R.G. Kelly, A. Baldini, D.
635 Zheng, and B.E. Morrow. 2021. Single cell multi-omic analysis identifies a Tbx1-
636 dependent multilineage primed population in murine cardiopharyngeal mesoderm. *Nat*
637 *Commun*. 12:6645.

638 Pulina, M.V., S.Y. Hou, A. Mittal, D. Julich, C.A. Whittaker, S.A. Holley, R.O. Hynes, and
639 S. Astrof. 2011. Essential roles of fibronectin in the development of the left-right
640 embryonic body plan. *Dev Biol*. 354:208-220.

641 Ramirez, A., and S. Astrof. 2020. Visualization and Analysis of Pharyngeal Arch Arteries
642 using Whole-mount Immunohistochemistry and 3D Reconstruction. *J Vis Exp*.

643 Ramsbottom, S.A., V. Sharma, H.J. Rhee, L. Eley, H.M. Phillips, H.F. Rigby, C. Dean, B.
644 Chaudhry, and D.J. Henderson. 2014. Vangl2-regulated polarisation of second heart
645 field-derived cells is required for outflow tract lengthening during cardiac development.
646 *PLoS Genet*. 10:e1004871.

647 Saga, Y., N. Hata, S. Kobayashi, T. Magnuson, M.F. Seldin, and M.M. Taketo. 1996.
648 MesP1: a novel basic helix-loop-helix protein expressed in the nascent mesodermal cells
649 during mouse gastrulation. *Development*. 122:2769-2778.

650 Saga, Y., S. Miyagawa-Tomita, A. Takagi, S. Kitajima, J. Miyazaki, and T. Inoue. 1999.
651 MesP1 is expressed in the heart precursor cells and required for the formation of a single
652 heart tube. *Development*. 126:3437-3447.

653 Sakai, T., K.J. Johnson, M. Murozono, K. Sakai, M.A. Magnuson, T. Wieloch, T.
654 Cronberg, A. Isshiki, H.P. Erickson, and R. Fassler. 2001. Plasma fibronectin supports
655 neuronal survival and reduces brain injury following transient focal cerebral ischemia but
656 is not essential for skin-wound healing and hemostasis. *Nat Med*. 7:324-330.

657 Singh, P., C. Carraher, and J.E. Schwarzbauer. 2010. Assembly of fibronectin
658 extracellular matrix. *Annu Rev Cell Dev Biol*. 26:397-419.

659 Sinha, T., D. Li, M. Theveniau-Ruissy, M.R. Hutson, R.G. Kelly, and J. Wang. 2015. Loss
660 of Wnt5a disrupts second heart field cell deployment and may contribute to OFT
661 malformations in DiGeorge syndrome. *Hum Mol Genet*. 24:1704-1716.

662 Sinha, T., B. Wang, S. Evans, A. Wynshaw-Boris, and J. Wang. 2012. Disheveled
663 mediated planar cell polarity signaling is required in the second heart field lineage for
664 outflow tract morphogenesis. *Dev Biol*. 370:135-144.

665 Soh, B.S., K. Buac, H. Xu, E. Li, S.Y. Ng, H. Wu, J. Chmielowiec, X. Jiang, L. Bu, R.A. Li,
666 C. Cowan, and K.R. Chien. 2014. N-cadherin prevents the premature differentiation of
667 anterior heart field progenitors in the pharyngeal mesodermal microenvironment. *Cell*
668 *Res*. 24:1420-1432.

669 Stefanovic, S., B. Laforest, J.P. Desvignes, F. Lescroart, L. Argiro, C. Maurel-Zaffran, D.
670 Salgado, E. Plaindoux, C. De Bono, K. Pazur, M. Theveniau-Ruissy, C. Beroud, M.
671 Puceat, A. Gavalas, R.G. Kelly, and S. Zaffran. 2020. Hox-dependent coordination of
672 mouse cardiac progenitor cell patterning and differentiation. *Elife*. 9.

673 Suzuki, H.R., M. Solursh, and H.S. Baldwin. 1995. Relationship between fibronectin
674 expression during gastrulation and heart formation in the rat embryo. *Dev Dyn*. 204:259-
675 277.

676 Tsao, C.W., A.W. Aday, Z.I. Almarzooq, A. Alonso, A.Z. Beaton, M.S. Bittencourt, A.K.
677 Boehme, A.E. Buxton, A.P. Carson, Y. Commodore-Mensah, M.S.V. Elkind, K.R.
678 Evenson, C. Eze-Nliam, J.F. Ferguson, G. Generoso, J.E. Ho, R. Kalani, S.S. Khan, B.M.
679 Kissela, K.L. Knutson, D.A. Levine, T.T. Lewis, J. Liu, M.S. Loop, J. Ma, M.E. Mussolino,
680 S.D. Navaneethan, A.M. Perak, R. Poudel, M. Rezk-Hanna, G.A. Roth, E.B. Schroeder,
681 S.H. Shah, E.L. Thacker, L.B. VanWagner, S.S. Virani, J.H. Voecks, N.Y. Wang, K. Yaffe,
682 S.S. Martin, E. American Heart Association Council on, C. Prevention Statistics, and S.
683 Stroke Statistics. 2022. Heart Disease and Stroke Statistics-2022 Update: A Report From
684 the American Heart Association. *Circulation*:CIR0000000000001052.

685 Turner, C.J., K. Badu-Nkansah, and R.O. Hynes. 2017. Endothelium-derived fibronectin
686 regulates neonatal vascular morphogenesis in an autocrine fashion. *Angiogenesis*.
687 20:519-531.

688 Wang, X., and S. Astrof. 2016. Neural crest cell-autonomous roles of fibronectin in
689 cardiovascular development. *Development*. 143:88-100.

690 Wang, X., and S. Astrof. 2017. Isolation of Mouse Cardiac Neural Crest Cells and Their
691 Differentiation into Smooth Muscle Cells. *Bio Protoc*. 7.

692 Zhang, Q., D. Carlin, F. Zhu, P. Cattaneo, T. Ideker, S.M. Evans, J. Bloomekatz, and N.C.
693 Chi. 2021. Unveiling Complexity and Multipotentiality of Early Heart Fields. *Circ Res*.
694 129:474-487.

695 Zimmerman, S.P., S.B. Asokan, B. Kuhlman, and J.E. Bear. 2017. Cells lay their own
696 tracks - optogenetic Cdc42 activation stimulates fibronectin deposition supporting
697 directed migration. *J Cell Sci*. 130:2971-2983.
698

Figure 1

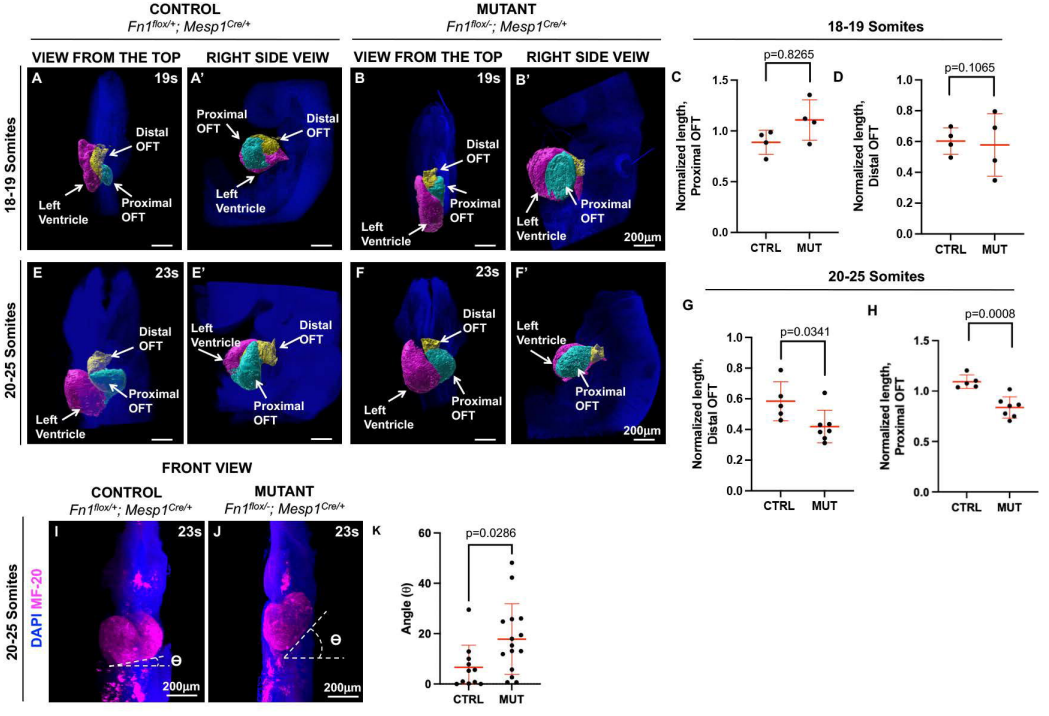

Figure 1. The expression of Fn1 in Mesp1 lineage is required for the OFT elongation.
Fn1$^{flox/+}$; Mesp1$^{Cre/+}$ (Control) and Fn1$^{flox/-}$; Mesp1$^{Cre/+}$ (Mutant) embryos were dissected at E9.5 and staged according to somite number. **A-D.** Embryos between 18-19 somites. n=5 controls and 4 mutants. **E-H.** Embryos between 20-25 somites, n= 5 control and 7 mutant embryos. Imaris was used to surface distal OFT (yellow), proximal OFT (turquoise), and the left ventricle and atria (pink). **C-D, G-H.** The length of the distal and proximal OFT in each embryo was normalized to the height of the left ventricle, to control for embryo size
I-J. Fn1$^{flox/+}$; Mesp1$^{Cre/+}$ (Control) and Fn1$^{flox/-}$; Mesp1$^{Cre/+}$ (Mutant) embryos were dissected at E9.5 (20-25s) and stained with DAPI and the MF-20 antibody. **K**. Quantification of angles in controls and mutants as shown in **I-J**. n= 9 controls and 13 mutants. Means (horizontal bars) and standard deviations (error bars) are displayed; p was calculated using 2-tailed, unpaired Student's t test. OFT-outflow tract, MF-20- antibody detecting sarcomeric myosin heavy chain.

Figure 2

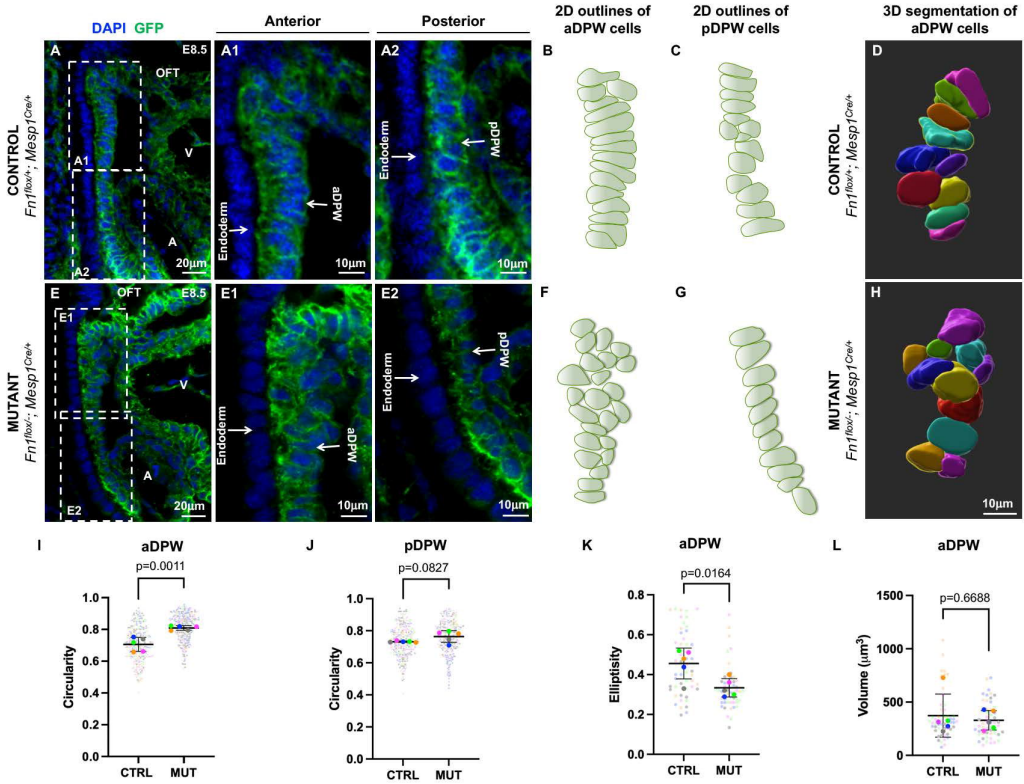

Figure 2. The expression of Fn1 in the mesoderm is important for the regulation of cell shape in the anterior DPW at E8.5. **A.** Fn1$^{flox/+}$; Mesp1$^{Cre/+}$ (Control) and **E.** Fn1$^{flox/-}$; Mesp1$^{Cre/+}$ (Mutant) embryos were dissected at E8.5 (9-11s) and stained to detect GFP (green) and nuclei (DAPI, blue). Regions marked by dashed rectangles in **A, B** are magnified in **A1-E1** and **A2-E2**. **B-C, F-G.** Outlines of aDPW and pDPW cells. **D-H.** 3D shapes of aDPW cells. **I-L.** Shape analyses. Small dots mark a data point from each cell, large dots mark average per embryo. Data points from one embryo are marked with the same color. **I-J**. Cell circularity. **I.** 320 cells from 5 control and 367 cells from 5 mutant embryo were analyzed. **J.** 311 cells from 5 control and 326 cells from 5 mutant embryo were analyzed. **K-L.** Ellipticity and volume of aDPW cells. n=51 cells from 5 control and 50 cells from mutant embryos were analyzed. Means (horizontal bars) and standard deviations (error bars) are displayed; p was calculated using 2-tailed, unpaired Student's t test. OFT-outflow tract, aDPW-anterior dorsal pericardial wall, pDPW-posterior dorsal pericardial wall, A-atrium, V-ventricle.

Figure 3

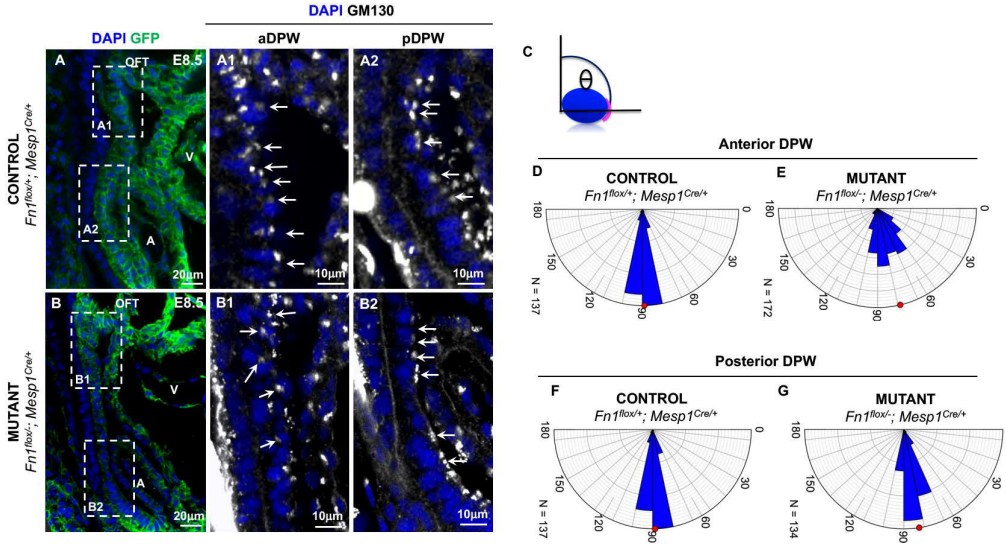

Figure 3. Expression of Fn1 in the mesoderm regulates Golgi apparatus orientation in the anterior DPW. A-B. Fn1$^{flox/+}$; Mesp1$^{Cre/+}$ (Control) and **C-D.** Fn1$^{flox/-}$; Mesp1$^{Cre/+}$ (Mutant) embryos were dissected at E8.5 (9-11s), and stained to detect GFP (green), GM130 (white), and nuclei (DAPI, blue). **A1-B1.** Magnification of the aDPW. **A2-B2**. Magnification of the pDPW. **D-G.** Semicircular histograms show the distribution of the Golgi orientation angles in SHF cells, measured as is indicated in **C**. N=number of cells analyzed. 3 different control and mutant were analyzed. OFT-outflow tract, aDPW-anterior dorsal pericardial wall, pDPW-posterior dorsal pericardial wall, A-atrium, V-ventricle

Figure 4

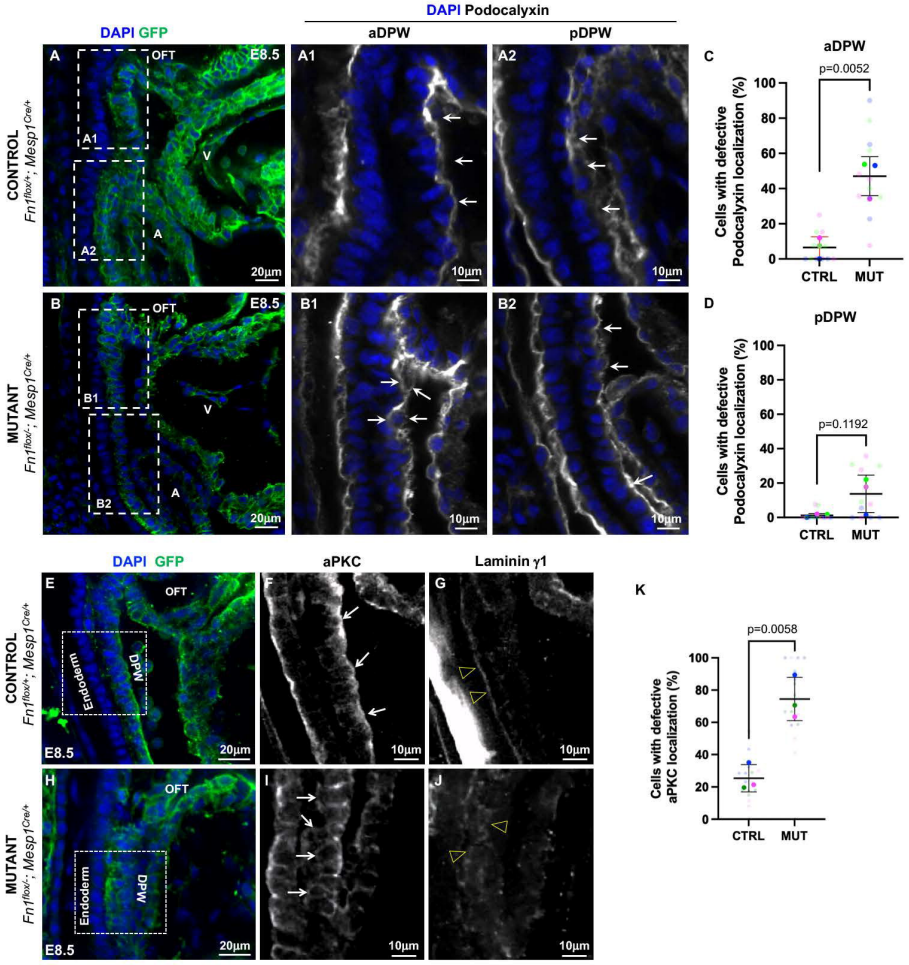

Figure 4. Expression of Fn1 in the mesoderm regulates cell polarity in the anterior DPW. **A.** Fn1$^{flox/+}$; Mesp1$^{Cre/+}$ (Control) and **B.** Fn1$^{flox/-}$; Mesp1$^{Cre/+}$ (Mutant) embryos were dissected at E8.5 (9-11s), and stained to detect GFP (green), podocalyxin (white), and nuclei (DAPI, blue). Boxes in **A** and **B** were expanded in **A1** and **B1** to show the anterior DPW and in **A2** and **B2** to show the posterior DPW. Arrows in **A1** indicate cells with normal apical localization of podocalyxin. Arrows in **B1** show a defective basolateral localization of podocalyxin in mutants. **A2, B2.** Podocalyxin is localized apically in the posterior DPW. **C-D** Quantification of cells with defective podocalyxin localization in the anterior and posterior DPW. **C.** 148 cells in the aDPW from 3 controls and 224 cells in aDPW from 3 mutants were analyzed. **D.** 149 cells in the pDPW from 3 controls and 182 cells in the pDPW from 3 mutants were analyzed. Each small dot represents data from one slice, and each large dot is an average of all slices per embryo. Data from the same embryo is marked by the same color.

E-G. Fn1$^{flox/+}$; Mesp1$^{Cre/+}$ (Control) and **H-J.** Fn1$^{flox/-}$; Mesp1$^{Cre/+}$ (Mutant) embryos were dissected at E8.5 (7-8s), and stained for GFP (green), aPKC, laminin γ1, and nuclei (DAPI, blue). Arrows in **F** point to apical localization of aPKC in control SHF cells. **I** Arrows point to defective basolateral localization of aPKC in mutants. Arrowheads in **G** point to basal localization of laminin γ1 in controls and in **J** to disorganized localization of laminin γ1 in mutants. **K.** Quantification of cells in which aPKC was re-distributed away from the apical surface. DPW cells from 5 different slices were evaluated in 3 control and 3 mutant embryos. Each small dot represents data from one slice, and each large dot is an average of all slices per embryo. Data from the same embryo is marked by the same color.

Means (horizontal bars) and standard deviations (error bars) are displayed; p was calculated using 2-tailed, unpaired Student's t test. OFT-outflow tract, aDPW-anterior dorsal pericardial wall, pDPW-posterior dorsal pericardial wall, A-atrium, V-ventricle.

Figure 5

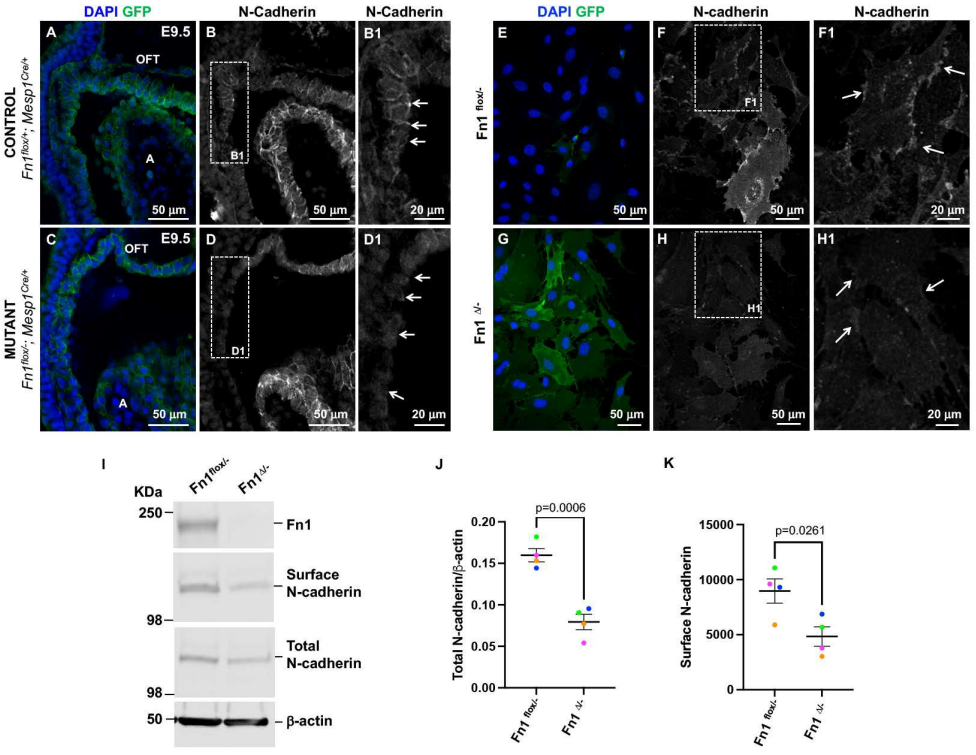

Figure 5. Mesodermal Fn1 regulates the expression of N-Cadherin at cell-cell junctions in the DPW. A-B. Fn1$^{flox/+}$; Mesp1$^{Cre/+}$ (Control) and **C-D.** Fn1$^{flox/-}$; Mesp1$^{Cre/+}$ (Mutant) embryos were dissected at E9.5 (21-26s) and stained to detect GFP (green), N-cadherin (white) and nuclei (DAPI, blue). Junctional N-Cadherin is enriched in the anterior DPW (boxed region in **B**). Boxes in **B-D** are expanded in **B1-D1.** Arrows point to DPW. **E-H.** Immunostaining to detect GFP (green), N-cadherin (white) and nuclei (DAPI, blue) in Fn1$^{\Delta/-}$ (Fn1-null) and Fn1$^{flox/-}$ (Fn1-het) MEFs. Boxes in **F-H** are expanded in **F1-H1.** Arrows point to N-cadherin at cell junctions in control MEFs (**F1**) and to the absent N-cadherin in Fn1-null MEFs (**H1**). **I.** Western blot analysis of total cell lysates and cell surface proteins. Positions of molecular mass markers is indicated on the left. **J-K**. Densitometrical quantification of immunoblot signals. n = 4 for each genotype. Each experiment is represented by a dot of different color. Means (horizontal bars) and standard deviations (error bars) are displayed, 2-tailed, unpaired Student's t test was used to determine p values. OFT-outflow tract, A-atrium.

Figure 6

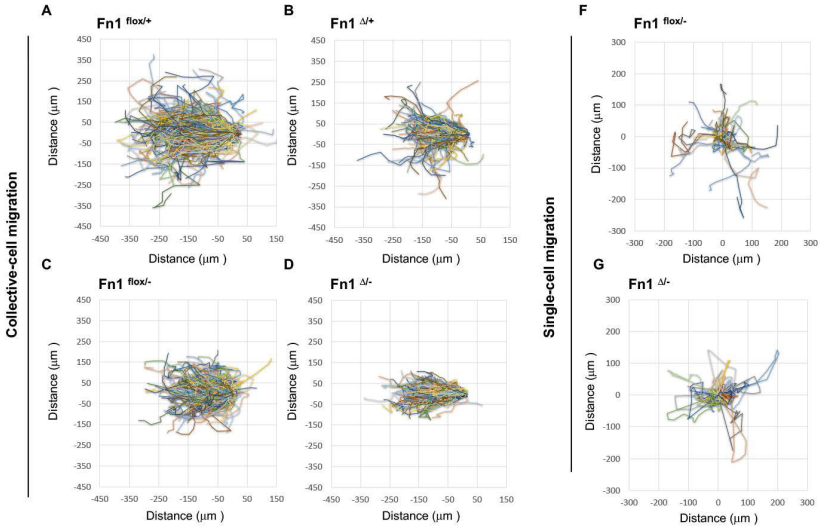

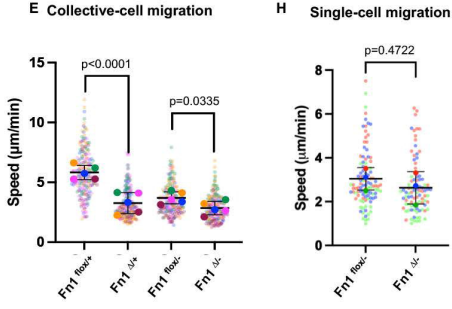

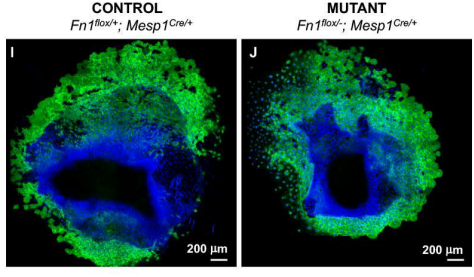

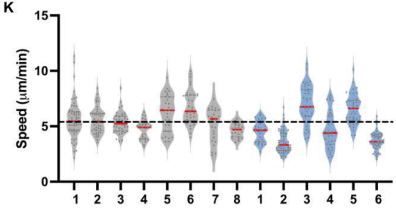

Figure 6. Fn1 regulates collective-cell migration. A-E. Confluent monolayers were scratched and trajectories and speed of cells in the monolayers were measured, 30 cells were evaluated per condition, n=5 independent experiments. **F-H**. Trajectories and speed of individually-migrating cells in sparse cultures were measured, 30 cells were evaluated per condition, n=3 independent experiments. Means (horizontal bars) and standard deviations (error bars) are displayed; p-values were calculated using 2-tailed, unpaired Student's t test. Small dots mark the speed of each each cell, large dots of the same color mark the average speed in each experiment. **I-K.** Pharyngeal explants. Embryos were dissected at E8.5, head, heart, and embryonic region posterior to the heart were removed, and the remaining piece was placed on a collagen I-coated ibidi plate at 37ºC for 24 h, and cells were then imaged for 16 hours. **K.** Cell speed. Each dot marks one cells, 25-54 cells were tracked in each explant. Red lines mark the average speed of cells in each explant. The black dashed line marks the overall average cell speed in control explants.

Figure 7

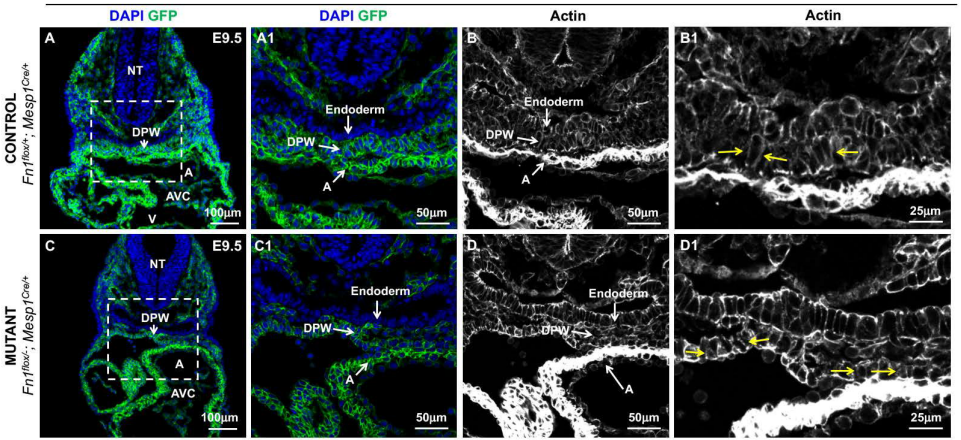

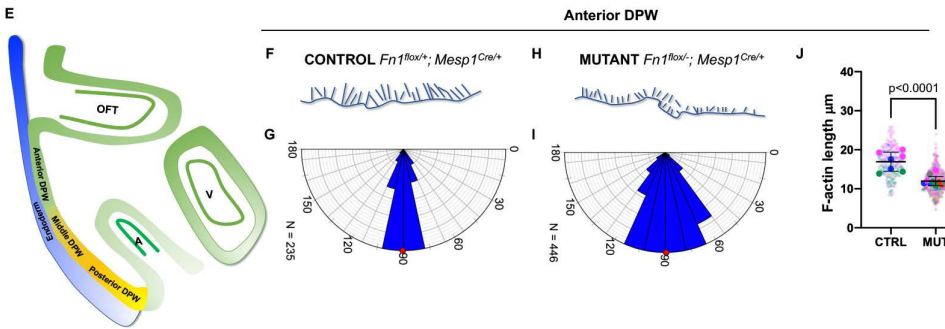

Figure 7. Mesodermal Fn1 regulates the length and organization of actin in the anterior DPW. A-B1. Fn1$^{flox/+}$; Mesp1$^{Cre/+}$ (Control) and **C-D1.** Fn1$^{flox/-}$; Mesp1$^{Cre/+}$ (Mutant) embryos were dissected at E9.5 (21-26s), and transverse cryosections from the anterior DPW were stained to detect GFP (green), F-actin (white), and nuclei (DAPI, blue). Yellow arrows point at F-actin in the SHF. **E.** Schematic representation of regions in the DPW. **F-H.** Traces of F-actin in control and mutants. **G-I.** Angles made by F-actin filaments relative to cells' apical surface were measured. **J.** Quantification of the F-actin length in the anterior DPW; 235 cells from 3 controls and 417 cells from 5 mutants were examined. Small dots mark F-actin length of individual cells and large dots mark the average per slice. Slices from each embryo are the same color. Means (horizontal bars) and standard deviations (error bars) are displayed; p was calculated using 2-tailed, unpaired Student's t test. DPW-dorsal pericardial wall, A-atrium, NT-Neural tube, AVC-atrioventricular canal, OFT-outflow tract, V-ventricle

Figure 8

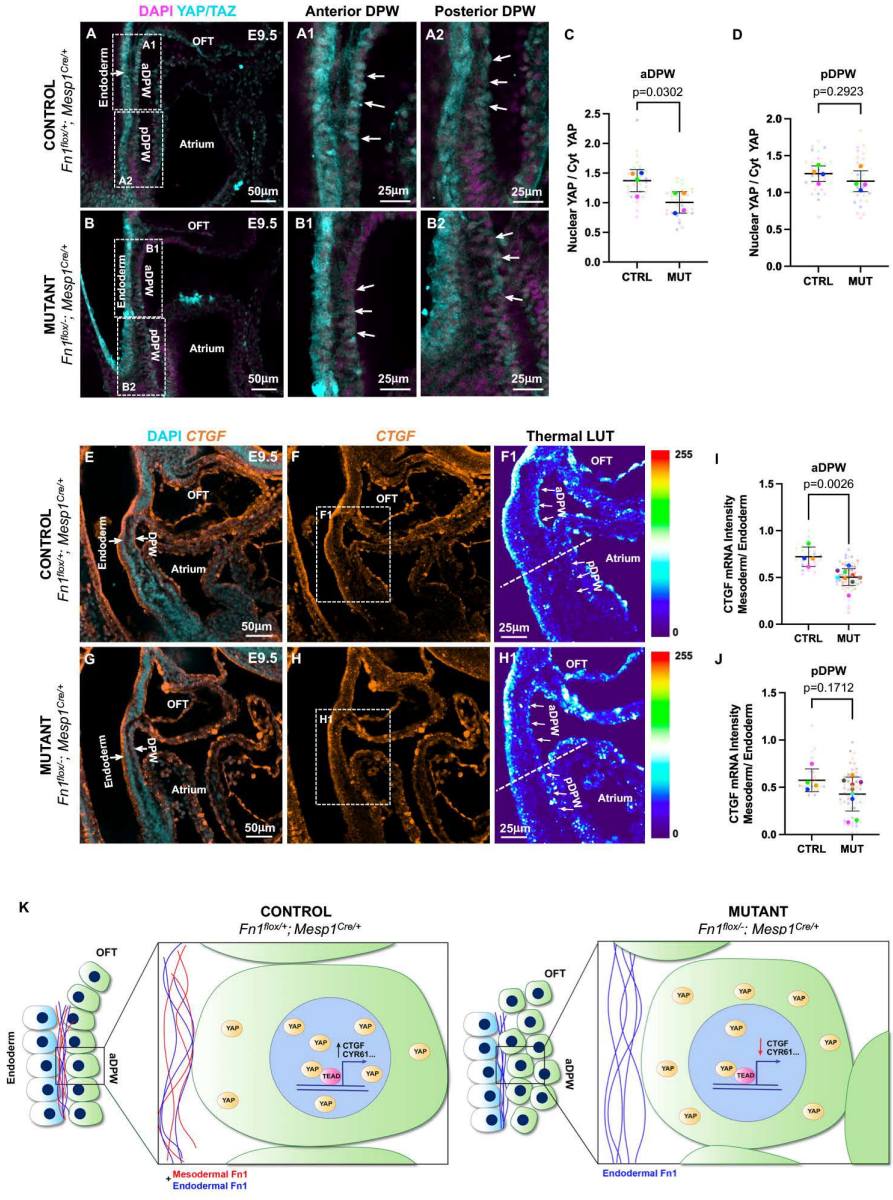

Figure 8. Mesodermal Fn1 regulates nuclear translocation and transcriptional activity of YAP. A. Fn1$^{flox/+}$; Mesp1$^{Cre/+}$ (Control) and **B.** Fn1$^{flox/-}$; Mesp1$^{Cre/+}$ (Mutant) embryos were dissected at E9.5 (23-26s) and stained to detect nuclei (DAPI, magenta) and YAP (cyan). Regions outlined by dashed rectangles are expanded in **A1, B1** (anterior DPW) and **A2, B2** (posterior DPW). **C-D**. Quantification of the intensity ratio between nuclear and cytosolic YAP in the aDPW and pDPW. 7-8 optical slices from 4 controls and 7-8 optical slices from 4 mutant embryos were analyzed. Each small dot represents one slice, and each large dot is an average of all slices per embryo. Data from the same embryo is marked by the same color. **E-F.** Fn1$^{flox/+}$; Mesp1$^{Cre/+}$ (Control) and **G-H.** Fn1$^{flox/-}$; Mesp1$^{Cre/+}$ (Mutant) embryos were dissected at E9.5 (23-26s) and labeled to detect *CTGF mRNA* (Orange) and nuclei (cyan). Rectangles in **F-H** are expanded in **F1-H1** and color-coded according to fluorescence intensity (scale is on the right). **I.** Quantification of *CTGF* mRNA fluorescence intensity ratio between the aDPW (mesoderm) and anterior endoderm **J.** Quantification of *CTGF* mRNA fluorescence intensity ratio between the pDPW (mesoderm) and posterior endoderm. n= 6 optical slices from 4 control and 9 mutant embryos were evaluated. Each small dot represents one slice, and each large dot is an average of all slices per embryo. Data from the same embryo is marked by the same color. Means (horizontal bars) and standard deviations (error bars) are displayed, 2-tailed, unpaired Student's t test was used to determine p values. **K**. Summary. In the presence of both the mesodermal and endodermal Fn1, YAP is localized to the nuclei and mediates transcription of *CTGF mRNA* in the anterior DPW. In the absence of mesodermal Fn1, nuclear translocation and activity of YAP are decreased. aDPW- anterior dorsal pericardial wall, pDPW-posterior dorsal pericardial wall, OFT-outflow tract.

Figure 9

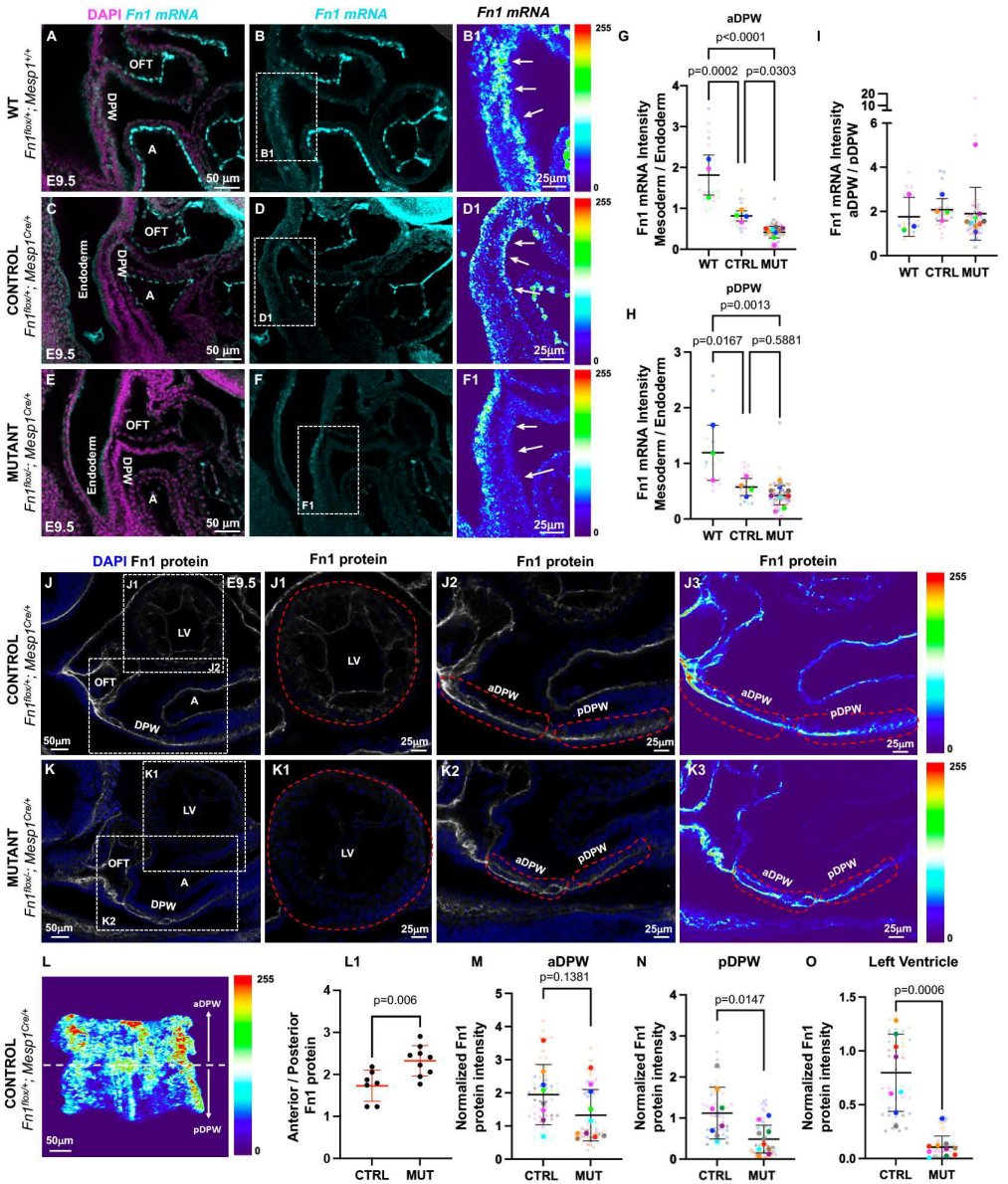

Figure 9. Expression patterns of *Fn1 mRNA* and protein in controls and mutants. **A-H.** Expression of *Fn1 mRNA*. **A-B** Fn1$^{flox/+}$; Mesp1$^{+/+}$ (WT), **C-D.** Fn1$^{flox/+}$; Mesp1$^{Cre/+}$ (Control), and **E-F.** Fn1$^{flox/-}$;Mesp1$^{Cre/+}$ (Mutant) embryos were dissected at E9.5 (23-26s) and labeled with DAPI (magenta) and anti-sense Fn1 probe (turquoise). Regions outlined by the dotted rectangles in B,D,F are expanded in **B1,D1** and **F1** and color-coded according to fluorescence intensity (intensity scale is on the right). White arrows point to the aDPW. **G.** Quantification of the *Fn1 mRNA* intensity ratio between the aDPW (mesoderm) and anterior endoderm. **H.** Quantification of *Fn1 mRNA* intensity ratio between the pDPW (mesoderm) and posterior endoderm. **I.** *Fn1 mRNA* Intensity ratio between aDPW and pDPW. 6 different slices from 3 WT, 4 control and 9 mutant embryos were analyzed.
J. Fn1$^{flox/+}$; Mesp1$^{Cre/+}$ (Control) and **K.** Fn1$^{flox/-}$; Mesp1$^{Cre/+}$ (Mutant) embryos were dissected at E9.5 (22-26s) and stained to detect Fn1 protein (white) and nuclei (DAPI, blue). Regions outlined by rectangles are expanded in **J1-J3** and **K1-K3**. **J1, K1**. Fn1 protein expression in the left ventricle. **J2, K2** Fn1 protein expression in the DPW color-coded according to fluorescence intensity in **J3, K3**. **L.** Ventral view of the DPW, Fn1 expression is color-coded according to fluorescence intensity. **L1.** Quantification of Fn1 protein intensity ratio between aDPW and pDPW, according to **L.** Each dot marks one embryos. **M-O.** Quantification of Fn1 intensity in the aDPW, pDWP and LV regions outlined by the red dash lines in **J1-K3**, normalized by DAPI intensity; 7 optical slices from 8 control and 10 mutant embryos were evaluated. Each small dot represents one slice, and each large dot is an average of all slices per embryo. Data from the same embryo is marked by the same color. Means (horizontal bars) and standard deviations (error bars) are displayed, 2-tailed, unpaired Student's t test was used to determine p values. aDPW-anterior dorsal pericardial wall, pDPW- posterior dorsal pericardial wall, OFT-outflow tract, A-atrium, LV-left ventricle.

Figure 10

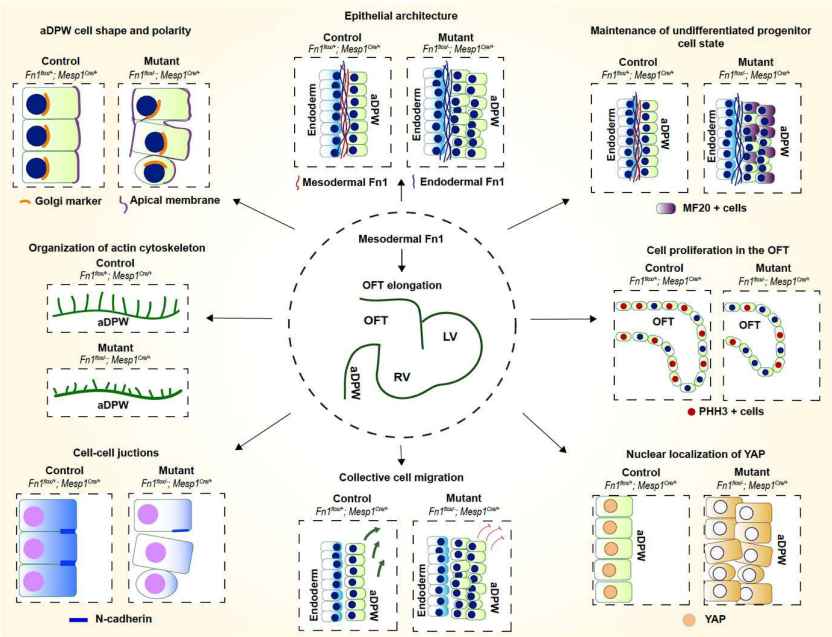

Figure 10. Summary of cellular and molecular processes regulated by mesodermal Fn1 in the DWP. Fn1 synthesized by the mesoderm is a central regulator of epithelial properties in the anterior dorsal pericardial wall (aDPW) and outflow tract elongation.